Title:

From highly polluted Zn-rich acid mine drainage to non-metallic waters: implementation of a multi-step alkaline passive treatment system to remediate metal pollution.

Authors:

Francisco Macías[a*], Manuel A. Caraballo[a,b], Tobias S. Rötting[c] ,Rafael Pérez-López[a,d]
José Miguel Nieto[a], Carlos Ayora[d]

[a] *Geology Department, University of Huelva, Campus "El Carmen", E-21071 Huelva, Spain.*

[b] *Department of Geosciences, Virginia Tech, Blacksburg, VA 24061, U.S.A.*

[c] *Department of Geotechnical Engineering and Geosciences, Technical University of Catalonia UPC-Barcelona Tech, Jordi Girona 1-3, D2-006, E-08034 Barcelona, Spain.*

[d] *Institute of Environmental Assessment and Water Research, CSIC, Jordi Girona 18, E-08034 Barcelona, Spain.*

*corresponding author:

francisco.macias@dgeo.uhu.es

Tel.: +34-95-921-9834; fax: +34-95-921-9810

Abstract

Complete metal removal from highly-polluted acid mine drainage was attained by the use of a pilot multi-step passive remediation system. The remediation strategy employed can conceptually be subdivided into a first section where the complete trivalent metals removal was achieved by the employment of a previously tested limestone-based passive remediation technology followed by the use of a novel reactive substrate (caustic magnesia powder dispersed in a wood shavings matrix) obtaining a total divalent metals precipitation. This MgO-step was capable to abate high concentrations of Zn together with Mn, Cd, Co and Ni below the recommended limits for drinking waters. A reactive transport model anticipates that 1 m^3 of MgO-DAS (1 m thick x 1 m^2 section) would be able to treat a flow of 0.5 L/min of a highly acidic water (total acidity of 788 mg/L $CaCO_3$) during more than 3 years.

Keywords:

Acid mine drainage, metal pollution remediation, caustic magnesia, brucite, hydrozincite

1. Introduction

Acid mine drainage (AMD) is a major cause of water pollution arising from a poor management of mine activities, and it can be considered as the principal source of inorganic water pollution in mining districts (Younger et al., 2002). AMD polluted waters typically show low pH values, high acidity and high dissolved metal contents. The Iberian Pyrite Belt (IPB) can be considered on of the largest massive sulfide districts in the world. This region although mined since 3000 BC (Nocete et al., 2005), experimented its most extensive and intense mining period during 19th and 20th centuries with more than 100 active mines (Sáez et al., 1999). These abandoned and uncontrolled mines have left an enormous amount of pollution sources discharging AMD into the surrounding basins (Olías et al., 2004; Sarmiento et al., 2009a; 2011), particularly in the Odiel basin, where 427 km of its rivers are affected by AMD (Sarmiento et al., 2009b).

Iron and Al are two of the main contaminants present in the highly metal-polluted AMD typically found in the IPB, discharging to the Atlantic Ocean an average load of 7900 t/year Fe and 5800 t/year Al (Olías et al., 2006). Iron and Al present strong buffering systems in these waters (Sanchez España and Trevor, 2007), and both systems play a key role in the natural attenuation of AMD (Bigham and Nordstrom, 2000), and therefore, they must be taken into account in remediation attempts. Another important AMD constituent in the IPB is Zn which has an estimated discharge to the Atlantic Ocean of 3500 t/year, an almost 15% of global gross flux of continental Zn to the oceans (Olías et al., 2006; Sarmiento et al., 2009b). Also other divalent metals such as Mn, Cu, Cd, Co, Ni and Pb are present in these AMDs, all of them remain in solution until pH values of about 8.5 (Cortina et al., 2003), being this an important factor to be considered in remediation strategies.

Given this severe and widespread metal pollution, the IPB is regarded as a world-class example of AMD polluted region and as the perfect “field-laboratory” to develop and test remediation strategies applicable to a wide range of metal and metalloid pollutants, as well as others AMD polluted sites around the world where similar acid systems are present and efforts are made for its remediation (e.g. Strosnider et al., 2010; Caraballo et al., 2010; Behum et al., 2011).

Furthermore, the European Water Framework Directive 2000/60/EC exhorts the countries belonging to the European Union to achieve good ecological and chemical quality of all the European water bodies by 2015. However, in the context of the Odiel basin, due to its specific characteristics related to an ancient and uncontrolled AMD pollution, the regional authorities propose 2021 and 2027 as new deadlines for compliance with the Directive, depending on the severity of AMD pollution (BOJA 216, 2011).

AMD pollution sources in the Odiel basin, and in many other old mining districts in Europe and in the world, typically correspond to orphan sites. In addition, the lifetime of this pollution generation has been estimated to range between tens to hundreds or hundreds to thousands of years for coal or sulfide mining districts, respectively (Younger, 1997). Taking these considerations into account, passive treatment systems are proposed as the most feasible and sustainable remediation option from both economical and environmental points of view (PIRAMID-Consortium, 2003; Johnson and Hallberg, 2005).

Conventional passive treatment systems (e.g., anoxic limestone drains, reducing and alkalinity producing systems or limestone sand reactors) are based on limestone dissolution or a combination of limestone dissolution and sulfate reducing bacteria activity (Hedin et al., 1994; Jage et al., 2001; Watten et al., 2005). Their application, although successful in waters with low to intermediate metal concentrations (e.g., AMDs in coal mining districts), is highly discouraged in highly polluted AMDs because their high Fe and Al concentrations promote serious problems of clogging and loss of reactivity (Rötting, 2007). Moreover, the pH values reached by limestone dissolution are insufficient to precipitate divalent metals (Cortina et al., 2003) and the high Zn and Cu concentrations of these waters may result lethal for sulfate reducing bacteria (Cabrera et al., 2006).

During the last ten years, the investigations on remediation of highly metal-polluted AMD in the IPB have been focused on the used of a novel reactive substrate known as Dispersed Alkaline Substrate (DAS). The concept of DAS relies on a mixture of a fine-grained alkaline reagent (e.g., limestone sand or MgO powder) and an inert coarse matrix (e.g., wood shavings). Limestone-DAS is suitable for trivalent metal removal like Fe or Al (Caraballo et al., 2009a; 2011a, b), whereas MgO-DAS efficiently removes divalent metals like Zn, Mn, Cd, Co, Ni (Rötting et al., 2006; Caraballo et al., 2009b). In addition, a Natural Fe-Oxidizing Lagoon (NFOL) was designed and tested in the field to oxidize and remove some of the abundant Fe prior to the limestone-DAS treatment (Macías et al., 2012).

The aim of the present study is to obtain for the first time at the IPB a complete metal removal from a highly divalent and trivalent metal polluted AMD. To this end the hydrochemistry and mineralogy of the system will be discuss, paying special attention in the process involved in divalent metals removal. The most innovative aspect of the work is the implementation on a pilot scale of an MgO-based passive treatment focused on retention of divalent metals as the last step of a more complex system capable of treating highly polluted AMD. Moreover, the MgO-based treatment of divalent metal pollution in surface waters would not only be a local case study applied to acid mine water, but also circum-neutral mine water discharges with high divalent metal concentrations (e.g. Zn) can occur in mining areas where ore sulphides are hosted in carbonate rocks, for instance, Mississippi Valley-type lead-zinc deposits.

2. Materials and methods

2.1 Field remediation site

The passive pilot plant constructed at Monte Romero abandoned mine complex is located in the northern part of the IPB (SW Iberian Peninsula) (Fig. 1A). The first step is a natural pretreatment (NFOL), constructed near to the mine shaft where AMD groundwater emerges. The outflow of the NFOL is connected with the DAS passive treatment system by a pipe (Fig. 1B). A schematic view of the DAS system is shown in Figure 1C. The AMD is gravity forced through a downflow reactor of 3 m^3 in volume (T1) filled with limestone-DAS (80% (v/v) pine wood shavings and 20% (v/v) limestone sand) connected in series to two decantation ponds (D1, D2) of 6 m^3 in volume each with aeration cascades. AMD then flows through an identical limestone-DAS reactor (T2) and two further aeration cascades and decantation ponds (D3, D4). Finally, AMD flows through a reactive tank of 1m^3 in volume (T3) filled with MgO-DAS reactive mixture (80% (v/v) pine wood shavings and 20% (v/v) MgO powder). This tank was equipped with lateral sampling ports at 1, 5, 10, 15, 20, 30, 40, 60 and 80 cm depth for water sampling and measurement of physicochemical parameters. The MgO-DAS tank outflow discharges into the Monte Romero creek.

High purity limestone sand (99.9% $CaCO_3$) was purchased at a local quarry (nominal grain size 3-6 mm). Pine wood shavings (curved flakes with a maximum length of about 1.5 cm) were purchased at a local carpentry. MgO powder was supplied by Magnesitas

Navarras S.A. (Zubiri, NE-Spain). The bulk chemistry of the caustic magnesia type used in this study ("LIXIMAG") can be observed in Table 1, as well as the average grain size, which is typically less than 0.1 mm.

The chemical composition and physicochemical parameters range of the AMD at the mine shaft are shown in Table 2 (see Inflow). The mean flow rate emerging from the mine shaft and flowing through the NFOL pretreatment was 1.5 L/s. In order to adjust the inflow rate to the pilot scale of the treatment, the inflow at the first limestone-DAS tank was set to 1 L/min. The residence time (assuming a porosity of 50% in the reactive tanks) was 1.5 days for T1 and T2, 3 days for each decantation pond and 0.5 days for T3; i.e. a total of 15.5 days of residence time for the whole system.

2.2 Water and solid sampling

Water samples were taken every 15 days in the most representative points of the system: mine shaft, NFOL, inflow and outflow of the reactive tanks (T1-in, T1-out, T2-in, T2-out, T3-in and T3-out), and the outflows of the decantation ponds D1 and D3. Additional water samples were taken less frequently in the depth profile of T3 reactive tank. In all sampling campaigns the samples were filtered immediately after collection through 0.1 μm Millipore filters on Millipore syringe filters holders, acidified in the field to pH<1 with Suprapure HNO_3 and stored at 4ºC in sterile polypropylene containers until analysis.

Physical-chemical parameters were measured in the field using specific portable meters. The pH and redox potential were determined using a PH25 meter (Crison®) with Crison® electrodes, which was calibrated with 3 points (4.01, 7.00, 9.21) for pH and checked using 2 points (240 and 470 mV) for redox potential with Crison® standard solutions. Electrical conductivity and temperature were measured using a CM35 meter

(Crison®) with 3 calibration points (147 and 1413 µS/cm, and 12.88 mS/cm). Dissolved O_2 was measured with an auto-calibrating Hanna® meter. Gross alkalinity was determined by CHEMetrics® Total Titrets®, with a range of 10-100 or 100-1000 mg/L as $CaCO_3$ equivalents.

The drought season in the south of Spain promotes the cease of the AMD flow from the mine shaft at the end of the summer period. At this moment, a depth profile of T3 reactive tank was dug out to study the new-formed precipitates developed within the tank. Solid samples were taken at 0-6, 6-12, 12-20, 20-30, 30-40, 40-50, 50-60, 60-70 and 70-80 cm depth. Samples were preserved in plastic bags at room temperature in the dark during its transport to laboratory, where they were dried at room temperature to prevent mineral transformation.

2.3 Analytical techniques

Analyses of water samples were carried out in the Central Research Services of the University of Huelva by Inductively Coupled Plasma Atomic Emission Spectrometry (ICP-AES, Jobin Ybon Ultima2). The method used was designed to estimate major, minor and trace elements in waters affected by AMD (Tyler et al., 2004). Multi-elemental standard solutions prepared from single certified standards supplied by SCP SCIENCE were used for calibration. Certified Reference Materials (SRM-1640 NIST freshwater-type and inter-laboratory standard IRMM-N3 wastewater test material, European Commission Institute for Reference Materials and Measurements) were also analyzed. Detection limits were: 200 µg/L for Al, Fe, Mn, Mg and Si; 500 µg/L for Ca; 50 µg/L for Zn; 5 µg/L for Cu; 2 µg/L for As and 1 µg/L for Cd, Co, Cr, Ni, Pb, Sr and Ti, and the analytical error was lower than 5%.

Solid samples used for chemical analysis and X-ray diffraction (XRD) were crushed and quartered to obtain representative sub-samples, which were ground to <0.1 mm in an agate mill. XRD patterns were obtained with a Bruker D5005 X-ray Diffractometer with Cu Kα radiation. Diffractometer settings were 40 kV, 30 mA, a scan range of 3-65° 2θ, 0.02 2θ step size and 2.4-s counting time per step. To obtain the bulk chemistry of the T3 reactive tank precipitates, the sub-samples were digested with concentrated HNO_3. Metal concentrations of the different digestions were analyzed by ICP-AES.

Semi-quantitative chemical analysis and imaging of certain areas in the precipitates were obtained by the use of a JEOL JSM 5410 scanning electron microscope with an energy dispersive system (SEM-EDS). To gain a more accurate composition of some specific precipitates at the micro-scale, quantitative chemical analysis was performed with a JEOL JXA-8200 SuperProbe Electron Probe Micro-Analyzer (EPMA), using the fitted Wavelength-Dispersive Spectroscopy (WDS) equipment.

2.4 Reactive transport modeling

A 1-D reactive transport model of the T3 tank was created using the code RETRASO (Saaltink et al., 2004) to match the experimental observations on water chemistry and precipitates, corroborate the hypothesized geochemical processes, and extrapolate its future behaviour. Hydrogeochemical speciation and saturation indices were calculated using PHREEQC (Parkhurst and Appelo, 1999). Thermodynamic data for aqueous, mineral and gas phases were taken from the WATEQ4F database (Ball and Nordstrom, 1991). Data for hydrozincite was added according to Schindler et al. (1969), while brucite solubility was updated according to Xiong (2008).

3. Results and discussion

3.1 Passive treatment system hydrochemistry

The general hydrochemical behavior of the complete passive system with respect to the main major elements (Fe, Al, Ca, and Mg), alkalinity and pH is shown in Figure 2A.

An important Fe removal (165 mg/L) occurs between the mine shaft and T1-in due to the natural pretreatment in the NFOL. This high Fe removal can be attributed to different oxidation processes such as surface catalyzed oxidation of ferrous iron (SCOOFI; Jarvis and Younger, 2001; Younger et al., 2002) and biotic and abiotic oxidation and subsequent precipitation of schwertmannite (Macías et al., 2012). Additionally and in accordance to previous studies (Macías et al., 2009), 75% As presents in the NFOL is co-precipitated with schwertmannite. A decrease in AMD pH is observed in the transit of the water along the NFOL (Fig. 2), moving from 3.6 in the mine shaft to 2.4 in T1-in. This pH tendency can be explained by the release of protons due to Fe hydrolysis and precipitation of schwertmannite. This decrease in pH although could be understood as detrimental for the water quality is in fact beneficial because it enhances calcite dissolution in the first limestone-DAS tank (T1).

In T1, due to limestone dissolution, an increase in water pH (from 2.4 to 6), gross alkalinity (from 0 to 190 mg/L as $CaCO_3$ equivalents) and Ca concentration (from 221 to 608 mg/L) takes place (Fig. 2A). These changes in the water chemistry induce a strong trivalent metal removal within the tank, as it is reflected in the decrease from 100 to 20 mg/L and 90 to 6 mg/L Fe and Al, respectively (Fig. 2A). The residual As not retained in the NFOL as well as all Cu, Pb and Cr present in the AMD are completely removed within the first limestone-DAS tank due to adsorption and/or co-precipitation with the Fe and Al precipitates. A detailed explanation of the aforementioned processes and the Fe and Al mineral phases systematically found in this step of the passive treatment system can be obtained in Caraballo et al. (2009a; 2011a).

In the following decantation ponds (D1 and D2), almost all the remaining Fe is oxidized and precipitated in the form of schwertmannite leading to some alkalinity consumption (Fig. 2A). A slightly increase in water pH is also observed as a response of CO_2 degassing when the treated water contacts the atmosphere. In the second limestone-DAS tank and the third and fourth decantation ponds, the residual Fe and Al from the previous stage are now completely removed by the same processes mentioned for T1. Due to this preconditioning, the MgO-DAS tank (T3) treated an alkaline drainage with no trivalent metals and high concentration of divalent metals (Zn, Mn, Cd, Co and Ni). This absence of trivalent metals has been exposed as the best scenario to assure an optimal performance of the MgO-DAS (Caraballo et al., 2009b). As expected in the neutral pH conditions observed before T3, divalent metals concentration remained constant in the water with the exception of a slight increase in Zn concentration and a local Cd decrease within T2 (Fig. 2B). Zinc increase along the limestone sections of the system could be attributed to various factors: water evaporation in the ponds during the hot summer, high residence time of the system (inflow water does not have to match the water in the different sections of the treatment) and possible redissolution of Zn-particulate matter transported by the wind from the sulfide tailings in the proximities of the treatment. The process controlling Cd removal within T2 has been described as pH-dependent adsorption in previous studies (Caraballo et al., 2009b). As shown in Figure 2B and Table 2, a complete Zn, Mn, Cd, Co and Ni removal was attained after T3. The hydrochemistry and mineralogy developed within the MgO-DAS reactive tank will be discussed in the next section.

In order to synthesize the enormous water quality improvement achieved in the different sections of the passive treatment, a modified Ficklin diagram has been employed. This diagram is commonly employed to classify AMD waters on the basis of pH and metal concentration (Ficklin et al., 1992; Ríos et al., 2008). The employed classification ranges from high acidity (HA) to moderate alkalinity (MAlk) and from extreme metallic (EM) to low metallic (LM). The main pollutants, based on their concentration and toxicity, present on the highly metal polluted waters of Monte Romero has been introduced in the modified Ficklin diagram (Fig. 3). As can be observed, the initial AMD belongs to the moderate acidity-extreme metallic class and after the pH decrease in the NFOL evolves to high acidity-extreme metallic. In the sections of the treatment dominated by limestone dissolution the AMD changes to near neutral-extreme metallic. It is only after the MgO treatment when the water evolves to moderate alkalinity-low metallic. The high chemical quality obtained in the waters at the output of the system is offered in Table 2. As shown, when water chemistry after the treatment is compared with the limit values established for metals and toxic elements concentration in irrigation (Ayers and Westcot, 1994) and drinking waters (WHO, 2011), all the analyzed elements easily fulfill these recommendations.

3.2 Detailed water chemistry and mineralogy of the MgO-DAS reactive tank

The inflowing drainage in T3 reactive tank showed a pH of 6.5 (Figs. 2 and 4), and after MgO powder dissolution this pH was increased to 10 in the first 10 cm of the tank profile, maintaining this value to the bottom of the reactive substrate (Fig. 4).

Slightly under the surface of the reactive material (1 cm depth), the pH value is increased to 8.6, promoting a concomitant decrease in Zn, Co and Ni concentrations by 200 mg/L, 100 μg/L and 180 μg/L, respectively. Manganese and Cd are not retained on the surface of the substrate. The pH value at 5 cm depth is 9.7, leading to a reduction in Zn concentration to a value of 40 mg/L from the initial 430 mg/L in the inflowing drainage, as well as for Co and Ni that are reduced from 850 and 800 μg/L to 330 and

220 µg/L, respectively. However, Mn and Cd concentrations do not show an important decrease. Finally, at 10 cm depth the pH is stabilized close to a value of 10, promoting that Zn, Mn, Cd, Co and Ni are abated below detection levels (Fig. 4). This profile evolution of divalent metals concentrations is consistent with the pH-dependent variations of those metals concentrations proposed by Cortina et al. (2003).

Concerning the mineralogy of the neoformed phases within T3, Figure 5 shows a detailed view of Zn-rich precipitates distribution in the form of massive aggregates surrounding the wood shavings and the unreacted grains of the original substrate, and filling the voids left by the vegetal cells. These SEM images correspond to some samples obtained in the first 6 cm of the MgO-DAS in T3. From 6 cm depth to the bottom, the tank essentially contains unreacted MgO-DAS as can clearly be deduced if its chemical composition is compared with the one corresponding to the initial substrate (Table 3). Accordingly to these observations, T3 lifetime with an efficient performance could have been maintained during a much longer time if the mine shaft had not dried out.

The XRD pattern of the original substrate shows magnesite, ferroan magnesite, periclase, dolomite and portlandite as the main minerals detected. Gypsum was the only crystalline neoformed phase detected in the first 6 cm of the reactive material. Although Zn and Mn are the main constituents, on the basis of the bulk chemistry (Table 3), no Zn and/or Mn minerals could be precisely detected by XRD. The poor crystallinity and/or the small size of the crystallites of some neoformed phases limit the use of conventional XRD on those environments. From 10 cm to the bottom of the tank, brucite was detected as the only neoformed mineral within the tank, due to both periclase hydration and brucite precipitation.

EPMA analyses of more than 40 areas of some selected Zn-rich precipitates show a mean value of 76.22% Zn, with minor contents of Si, S, Mn, Ni and Co (Table 4). The slight Fe amount detected is probably inherited from ferroan magnesite in the initial substrate due to the absence of this element in the inflowing water. The sum of the main constituents (named as total in Table 4) quantified by EPMA presents an average of 84.88%. The chemical composition of those Zn-rich precipitates is reliably close to the expected one for hydroxy-carbonates of Zn (hydrozincite type) or Zn-hydroxides. Rötting et al. (2008) also identified these neoformed mineral phases in a column experiment treating Zn- and Mn- rich solutions using MgO-DAS.

In addition to the data presented in this study, a synchrotron light-induced micro analysis (combined μ-XRD and μ-XRF) has been recently performed to these precipitates. Hydrozincite [$Zn_5(CO_3)_2(OH)_6$] and a minor amount of loseyite [$(Mn,Zn)_7(CO_3)_2(OH)_{10}$] have been the only phases reliably identified as sinks for Zn and Mn, as well as for minor amounts of Co and Ni (Pérez-López et al., 2011). Even though no $Mn^{3+,4+}$-rich mineral could be identified, oxidation of Mn^{2+} to Mn^{3+} at high pH (Morgan, 1967) and subsequent manganite (γ-MnOOH) cannot be discarded.

3.3 Chemical and mineralogical control on MgO-DAS performance and time evolution

In the light of the hydrochemical and mineralogical data acquired in this study, it was decided to obtain a reactive transport model to fully understand the different processes controlling the MgO-DAS performance and also to estimate the lifetime that the reactive substrate would had if the shaft had not dried out.

According to the calculations, brucite is slightly supersaturated below 10 cm depth in the tank (SI = 0.2-0.6), and pH is lightly higher than expected for brucite control. As Ca was observed to increase with depth in the T3 tank (Fig. 4) and lime (CaO) was detected as a mineral constituent of the initial substrate, it was hypothesized that some hydrated lime ($Ca(OH)_2$) could be dissolving within the substrate, even though equilibrium was not reached. Moreover, gypsum (another neoformed phase detected by XRD within T3) was also, to some extent, supersaturated throughout the tank, so that gypsum precipitation could explain the observed decrease of sulfate concentrations with depth (Fig. 4). Rötting et al. (2008) had also identified gypsum precipitated in laboratory MgO-DAS columns treating water with a similar composition as the T3 inflow. Therefore, the possibility of brucite dissolution/precipitation, hydrated lime dissolution and gypsum precipitation was incorporated into the reactive transport model (Table 5).

The kinetic rate law for the dissolution of brucite was derived from data of various authors summarized by Pokrovsky and Schott (2004). The dissolution rates shown in figure 8 of their publication were approximated by the law:

$$r = 10^{-4}\, a_{H^+}^{0.45}\ \mathrm{mol \cdot m^{-2} \cdot s^{-1}} \qquad (1)$$

The amount *m* of mineral dissolved (mol/s) was calculated as:

$$m = A\, \mathbf{r}\, (1-\Omega) \qquad (2)$$

where *A* is the reactive surface area (m^2/m^3 of porous medium) and Ω is the saturation of the solution.

A finite-element mesh with 410 linear elements and a total length of 80 cm was used to represent the depth profile of the T3 MgO-DAS tank. Hydrozincite ($Zn_5(CO_3)_2(OH)_6$) and β-$Zn(OH)_2$ were set as potential Zn-sinks, and manganite (γ-MnOOH) as possible Mn-sink.

The autocatalytic oxidation of Mn^{2+} to Mn^{3+} was modelled after the kinetic law of Morgan (1967), as cited in Diem and Stumm (1984):

$$\frac{-d[Mn^{+2}]}{dt} = k'_1 [O_{2(aq)}]\,[OH^-]^2\,[Mn^{2+}] + k'_2\,[O_{2(aq)}]\,[OH^-]^2\,[MnO_x]\,[Mn^{2+}] \quad (3)$$

where $[Mn^{2+}]$, $[O_{2(aq)}]$ and $[OH^-]$ are dissolved concentrations (mol/L) of Mn^{2+}, oxygen and OH^-, respectively, $[MnO_x]$ is the concentration of Mn^{+3} reaction solid product (mol/L), k'_1 is the rate constant for homogeneous oxidation (4 10^{12} mol^3 L^{-3} day^{-1}) and k'_2 is the rate constant for heterogeneous oxidation (10^{18} mol^4 L^{-4} day^{-1}).

All the phases were allowed to precipitate in equilibrium once saturation is reached. The input solution was set to be in equilibrium with atmospheric O_2.

The values of the initial reactive surface areas of dissolving $Mg(OH)_2$ and $Ca(OH)_2$ were calibrated to match the measured depth profiles of Mg and Ca concentrations, and that of gypsum was adjusted to reproduce sulphate profiles (Table 5).

Using these parameters, the rest of pore-water concentrations, pH and the dissolved and precipitated solids calculated with the model match well with observations along the depths profile of the tank (Fig. 6A). Dissolved Mg concentration steeply increases in the first 4 cm of the substrate due to $Mg(OH)_2$ dissolution. Calcium concentration increases more slowly due to $Ca(OH)_2$ dissolution, causing pH to increase above $Mg(OH)_2$ saturation below 4 cm depth. Therefore, dissolved Mg decreases below this depth due to $Mg(OH)_2$ reprecipitation. The pH increase also causes Zn precipitation, as hydrozincite immediately at the substrate surface and as β-$Zn(OH)_2$ up to approximately 3 cm depth (Fig. 6B). Concentration of Mn^{2+} starts to decrease below the depth of the Zn-precipitation front, where pH is high enough to sufficiently accelerate Mn^{2+}-oxidation. The resulting Mn^{3+} immediately precipitates as manganite (Fig. 6B). As manganite has a low solubility at both alkaline and circumneutral pH (Eary, 1999), it does not redissolve even though the $Mg(OH)_2$-dissolution front moves downwards with time. Due to Ca increase, gypsum precipitates along the depth profile of the tank, and dissolved sulphate decreases accordingly.

The numerical model was also used to extrapolate the “lifetime” of the MgO tank. Assuming uniform flow, the MgO-DAS in the tank (1 m^3) would have been able to treat the Monte Romero AMD at a flow rate of 0.5 L/min during approximately 3.4 years before Mn or Zn breakthrough at the tank outlet. However, this modelled hypothesis needs to be corroborated in longer field trials.

4. Conclusions

The application of the natural pretreatment NFOL to oxidize Fe, coupled with limestone-DAS for trivalent metals retention (Fe and Al mainly) and finally MgO-DAS for Zn, Mn, Cd, Co and Ni elimination, has shown to be capable to achieve the complete metal removal from a highly metal-polluted AMD.

The reactive transport model extrapolations indicate that the 1 m^3 MgO-DAS tank is able to treat the Monte Romero AMD with a total acidity of 788 mg/L of $CaCO_3$ at a flow rate of 0.5 L/min during approximately 3.4 years before Mn or Zn breakthrough the tank outlet.

The widespread use of these passive plants in specific acid discharges could improve in a few years the ecological and chemical quality of the Odiel basin. The pilot plant design tested in Monte Romero abandoned mine is being considered by the regional authorities for full scale application at this AMD discharge. The same NFOL+DAS scheme is proposed to treat others acid discharges in the Odiel basin.

ACKNOWLEDGEMENTS

This research was financed by the Spanish Ministry of Education and Science through project CGL2010-21956-C02. F. Macías was financially supported by the Spanish Government with a FPI PhD fellowship. The assistance of Cristóbal Cantero for EPMA analysis at the Central Research Services of the University of Huelva is gratefully acknowledged. R. Pérez-López also thanks the Spanish Minister of Science and Innovation and the 'Ramón y Cajal' Subprogramme (MICINN-RYC 2011). Manuel A. Caraballo was financially supported by the Spanish Minister of Education and the Post-doctoral International Mobility Subprogramme I+D+i 2008-2011. The comments and helpful criticisms of an anonymous reviewer and the support of the Editors, Dr. Damià Barceló and Dr. Filip M.G. Tack, have considerably improved the original manuscript and are also gratefully acknowledged.

REFERENCES

Ayers RS, Westcot DW. Water Quality for agriculture. FAO Irrigation and Drainage Paper 29. Rev. 1, Rome, Italy; 1994.

Ball JW, Nordstrom DK. 1991. User's manual for WATEQ4F with revised thermodynamic database and test cases for calculating speciation of major, trace and redox elements in natural waters. U.S. Geological Survey, Water-Resources Investigation Report 1991; 91–183.

Behum PT, Lefticariu L, Bender KS, Segid YT, Burns AS, Pugh CW. Remediation of coal-mine drainage by a sulfate-reducing bioreactor: a case study from the Illinois coal basin USA. Appl Geochem 2011;26:162–166.

Bigham JM, Nordstrom DK. Sulphate minerals: Crystallography, geochemistry, and environmental significance. Mineralogical Society of America, Washington; 2000.

BOJA. Acuerdo de 2 de noviembre de 2011, del Consejo de Gobierno, por el que se aprueba inicialmente el Plan Hidrológico de la Demarcación Hidrográfica del Tinto, Odiel y Piedras. Boletín Oficial Junta de Andalucía 2000;216:9-11.

Cabrera G, Pérez R, Gómez JM, Ábalos A, Cantero D. Toxic effects of dissolved heavy metals on Desulfovibrio vulgaris and Desulfovibrio sp. strains. J Hazard Mater 2006;135:40-46.

Cánovas CR, Olías M, Nieto JM, Sarmiento AM, Ceron JC. Hydrogeochemical characteristics of the Tinto and Odiel Rivers (SW Spain). Factors controlling metal contents. Sci Total Environ 2007;373:363-382.

Caraballo MA, Rötting TS, Nieto JM, Ayora C. Sequencial extraction and DXRD applicability to poorly crystaline Fe- and Al-phase characterization from an acid mine water passive remediation system. Am Mineral 2009a;94:1029-1038.

Caraballo MA, Rötting TS, Macías F, Nieto JM, Ayora C. Field multi-step calcite and MgO passive system to treat acid mine drainage with high metal concentration. Appl Geochem 2009b;24:2301-2311.

Caraballo MA, Rötting TS, Silva V. Implementation of an MgO-based metal removal step in the passive treatment system of Shilbottle, UK: column experiments. J Hazard Mater 2010;181;923–930.

Caraballo MA, Macías F, Castillo J, Quispe D, Nieto JM, Ayora C. Hydrochemical performance and mineralogical evolution of a dispersed alkaline substrate (DAS) remediating the highly polluted acid mine drainage in the full scale passive treatment of Mina Esperanza (SW, Spain). Am Mineral 2011a;96:1270-1277.

Caraballo MA, Macías F, Rötting TS, Nieto JM, Ayora C. Long term remediation of highly polluted acid mine drainage: A sustainable approach to restore the environmental quality of the Odiel river basin. Env Poll 2011b;159:3613-3619.

Cortina JL, Lagreca I, De Pablo J, Cama J, Ayora C. Passive In Situ Remediation of Metal-Polluted Water with Caustic Magnesia: Evidence from Column Experiments. Environ Sci Technol 2003;37:1971-1977.

Diem D, Stumm W. Is Dissolved Mn^{2+} Being Oxidized by O^{-2} in Absence of Mn-Bacteria or Surface Catalysts. Geochim Cosmochim Ac 1984;48(7):1571-1573.

Eary LE. Geochemical and equilibrium trends in mine pit lakes. Appl Geochem 1999;14(8):963-987.

EC Decision 2000/60/EC. Council Decision of 23 October 2000 establishing a communitarian frame of action in the scope of water policy. Official Journal L 327, 22/12/2000, pp. 1-88.

Ficklin WH, Plumlee GS, Smith KS, McHugh JB. Geochemical classification of mine drainages and natural drainages in mineralized areas. Proceedings of the 7th International Symposium on Water Rock Interaction. Park City, Utah. 1992;381–384.

Hedin RS, Watzlaf GR, Nairn RW. Passive treatment of acid-mine drainage with limestone. J Environ Qual 1994;23:1338-1345.

Jage CR, Zipper CE, Noble R. Factors Affecting Alkalinity Generation by Successive Alkalinity-Producing Systems: Regression Analysis. J Environ Qual 2001;30:1015-1022.

Jarvis AP, Younger PL. Passive treatment of ferruginous mine waters using high surface area media. Water Res 2001;35(15):3643-3648.

Johnson DB, Hallberg KB. Acid mine drainage remediation options: a review. Sci Total Environ 2005;338;(1-2):3-14.

Macías F, Caraballo MA, Nieto JM, Ayora C, Rotting TS. Iron removal enhancement of a two step calcite passive treatment system at the Iberian Pyrite Belt. Geochim Cosmochim Ac 2009;73(13):A811-A811.

Macías F, Caraballo MA, Nieto JM, Rötting TS, Ayora C. Natural pretreatment and passive remediation of highly polluted acid mine drainage. J Environ Manage 2012;104:93-100.

Morgan JJ. Chemical equilibria and kinetic properties of manganese in natural waters. In: Principles and Applications of Water Chemistry, Faust, S. D., Hunter, J. V., Eds. Wiley, New York, pp. 561-624; 1967.

Nocete F, Álex E, Nieto JM, Sáez R, Bayona MR. An archaeological approach to regional environmental pollution in the south-western Iberian Peninsula related to Third millennium BC mining and metallurgy. J Archaeol Sci 2005;32:1566-1576.

Olías M, Nieto JM, Sarmiento AM, Cerón JC, Cánovas CR. Seasonal water quality variations in a river affected by acid mine drainage: the Odiel River (South West Spain). Sci Total Environ 2004;333(1-3):267-281.

Olías M, Cánovas CR, Nieto JM, Sarmiento AM. Evaluation of the dissolved contaminant load transported by the Tinto and Odiel rivers (South West Spain). Appl Geochem 2006;21:1733-1749.

Parkhurst DL, Appelo CAJ. User's Guide to PHREEQC (Version 2) A Computer Program for Speciation, Batch-Reaction, One-Dimensional Transport, and Inverse Geochemical Calculations, USGS Water-Resources Investigations, Denver, Colorado; 1999.

Pérez-López R, Macías F, Caraballo MA, Nieto JM, Román-Ross G, Tucoulou R, Ayora C. Mineralogy and Geochemistry of Zn-Rich Mine-Drainage Precipitates From an MgO Passive Treatment System by Synchrotron-Based X-ray Analysis, Environ Sci Technol 2011;45:7826-7833.

PIRAMID-Consortium. Engineering Guidelines for the Passive Remediation of Acidic and/or Metalliferous Mine Drainage and Similar Wastewaters. University of Newcastle, Newcastle Upon Tyne, UK; 2003.

Pokrovsky OS, Schott J. Experimental study of brucite dissolution and precipitation in aqueous solutions: Surface speciation and chemical affinity control. Geochim Cosmochim Ac 2004;68(1):31-45.

Ríos CA, Williams CD, Roberts CL. Removal of heavy metals from acid mine drainage (AMD) using coal fly ash, natural clinker and synthetic zeolites. J Hazard Mater 2008;156:23-35.

Rötting TS, Cama J, Ayora C, Cortina JL, De Pablo J. Use of Caustic Magnesia To Remove Cadmium, Nickel and Cobalt from Water in Passive Treatment Systems: Column Experiments. Environ Sci Technol 2006;40:6438-6443.

Rötting TS. Dispersed Alkaline Substrate (DAS): A novel option for the passive treatment of waters with high metal concentrations. Tesis Doctoral, Instituto de Ciencias de la Tierra “Jaume Almera”, CSIC; 2007.

Rötting TS, Ayora C, Carrera J. Improved Passive Treatment of High Zn and Mn Concentrations Using Caustic Magnesia (MgO): Particle Size Effects. Environ Sci Technol 2008;42:9370-9377.

Sáez R, Pascual E, Toscano M, Almodóvar GR. The Iberian type of volcano-sedimentary massive sulphide deposits. Mineralium Deposita 1999;34:549-570.

Saaltink MW, Battle F, Ayora C, Carrera J, Olivella S. RETRASO, a code for modelling reactive transport in saturated and unsaturated porous media. Geol Acta 2004;(3):235-251.

Sanchez España J, Trevor ML. The Behaviour of Iron and Aluminum in Acid Mine Drainage: Speciation, Mineralogy, and Environmental Significance. In: Thermodynamics, Solubility and Environmental Issues. Elsevier, Amsterdam, pp. 137-150; 2007.

Sarmiento AM, Nieto JM, Casiot C, Elbaz-Poulichet F, Egal M. Inorganic arsenic speciation at river basin scales: the Tinto and Odiel rivers in the Iberian Pyrite Belt, SW Spain. Environ Pollut 2009a;157:1202-1209.

Sarmiento AM, Nieto JM, Olías M, Cánovas, CR. Hydrochemical characteristics and seasonal influence on the pollution by acid mine drainage in the Odiel river Basin (SW Spain). Appl Geochem 2009b;24:697-714.

Sarmiento AM, DelValls A, Nieto JM, Salamanca MJ, Caraballo MA. Toxicity and potential risk assessment of a river polluted by acid mine drainage in the Iberian Pyrite Belt (SW Spain). Sci Total Environ 2011;409(22):4763-4771.

Schindler P, Reinert M, Gamsjäger H. Thermodynamics of Metal Carbonates 3. Solubility Constants and Free Formation Enthalpies of $ZnCO_3$ and $Zn_5(OH)_6(CO_3)_2$ at 25 Degrees. Helvetica Chimica Acta 1969;52(8):2327-2332.

Strosnider WH, Nairn RW. Effective passive treatment of high-strength acid mine drainage and raw municipal wastewater in Potosí, Bolivia using simple mutual incubations and limestone. J Geochem Explor 2010;105:34–42.

Tyler G, Carrasco R, Nieto JM, Pérez R, Ruiz MJ, Sarmiento, AM. Optimization of major and trace element determination in acid mine drainage samples by ultrasonic nebulizer-ICP-OES (USN-ICP-OES). Pittcon conf., Chicago, USA; 2004.

Xiong Y. Thermodynamic Properties of Brucite Determined by Solubility Studies and Their Significance to Nuclear Waste Isolation. Aquat Geochem 2008;14(3):223-238.

Younger PL. The longevity of mine water pollution: a basis for decision-making. Sci Total Environ 1997;194-195(0):457-466.

Younger PL, Banwart SA, Hedin RS. Mine Water - Hydrology, Pollution, Remediation. Dordrecht; Kluwer Academic Publishers; 2002.

Watten BJ, Sibrell PL, Schwartz MF. Acid neutralization within limestone sand reactors receiving coal mine drainage. Env Poll 2005;137:295-304

WHO. Guidelines for drinking-water quality, fourth edition. World Health Organization.http://www.who.int/water_sanitation_health/publications/2011/dwq_guidelines/en/index.html [Last accessed January 17, 2011].

FIGURE CAPTIONS

Figure 1. General (A) and detailed (B) field site location, and schematic view of the DAS passive treatment system (C).

Figure 2. Fe, Al, Ca, Mg (mg/L), alkalinity (mg/L as $CaCO_3$ equivalents) and pH (A), and Zn, Mn (mg/L), Cd, Co, Ni (µg/L) and pH (B) distribution along the main representative points of the treatment.

Figure 3. Modified Ficklin diagram for the different steps of the treatment. HA: high acidity, MA: moderate acidity, NN: near neutral, MAlk: moderate alkalinity, EM: extreme metallic, HM: high metallic, LM: low metallic. Data obtained from five sampling campaigns.

Figure 4. Zn, Mg, Ca, Mn, SO_4, Cd, Co, Ni and pH hydrochemical depth profile in the MgO-DAS reactive tank.

Figure 5. SEM images of the Zn-rich precipitates developed within the MgO-DAS reactive tank.

Figure 6. Depth profiles for Zn, Mn, Mg, Ca, SO_4 (mg/L) concentrations and pH (A), and mineral mass change (mol/kg) for brucite, gypsum, manganite, hydrozincite, β-$Zn(OH)_2$ and portlandite (B). Symbols indicate experimental data (real) and lines represent data obtained in the reactive transport modelling (model).

TABLES

Table 1. Bulk composition and particle size distribution of the caustic magnesia used in the T3 MgO-DAS tank. (Source: Magnesitas de Navarra S.A., LIXIMAG).

Table 2. Chemical composition and physicochemical parameters of the inflow (mine shaft) and outflow (discharge of T3) in the passive treatment of Monte Romero. Data obtained from five sampling campaigns.

Table 3. Bulk chemistry (mg/g) of the MgO-DAS filling substrate in the T3 reactive tank after the treatment commission.

Table 4. EPMA analysis (wt%) of the neoformed Zn-rich phases in the first 6 cm of depth in T3 reactive tank. A basic statistic (mean, maximum, minimum and standard deviation) for 46 analysis points is shown.

Table 5. Kinetic-equilibrium reactions and initial reactive surface of the MgO-DAS used in the reactive transport model.

Figure 1

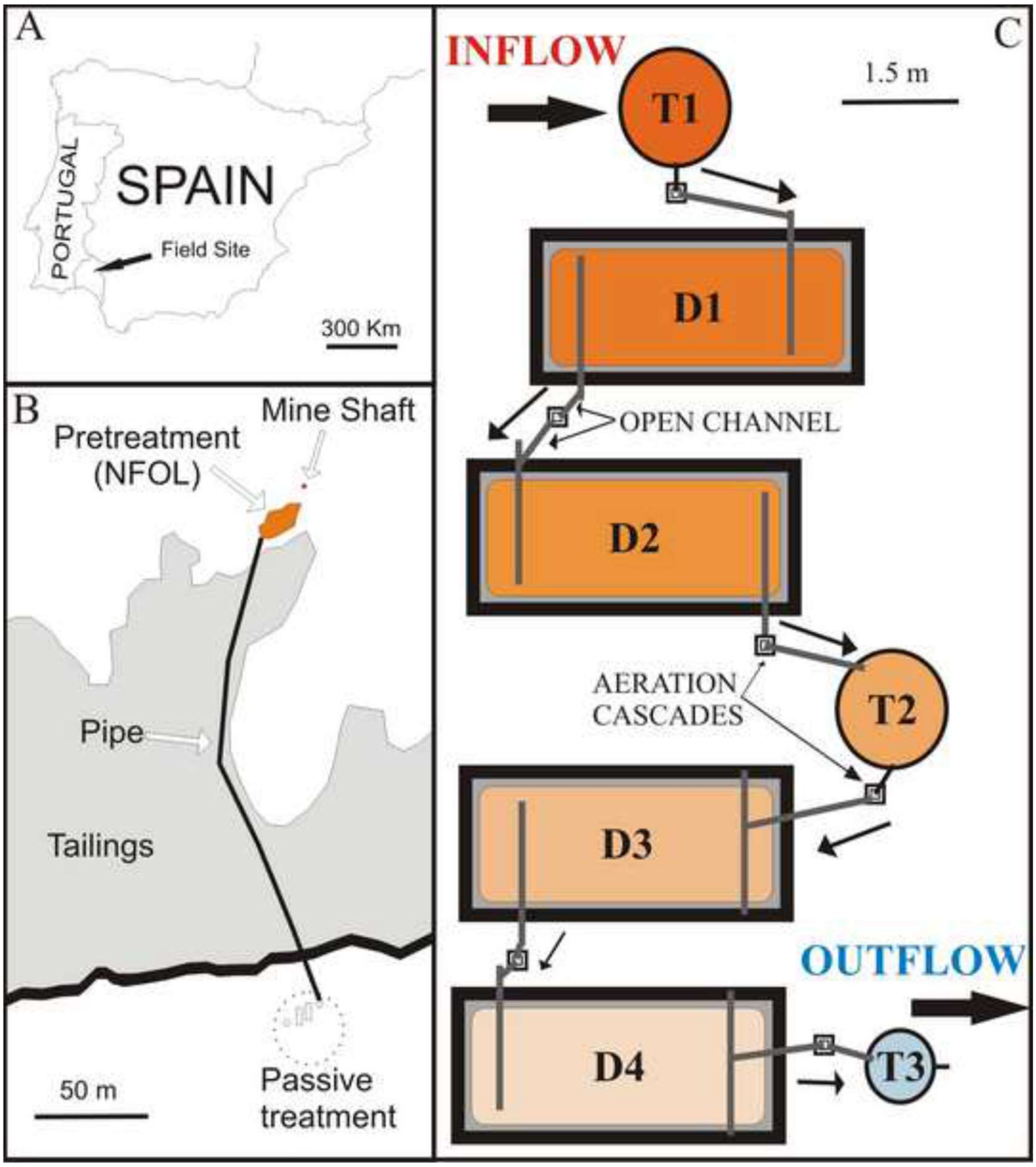
A
SPAIN
PORTUGAL
Field Site
300 Km
B
Mine Shaft
Pretreatment (NFOL)
Pipe
Tailings
Passive treatment
50 m
C
INFLOW
T1
1.5 m
D1
OPEN CHANNEL
D2
AERATION CASCADES
T2
D3
OUTFLOW
D4
T3

Figure 2

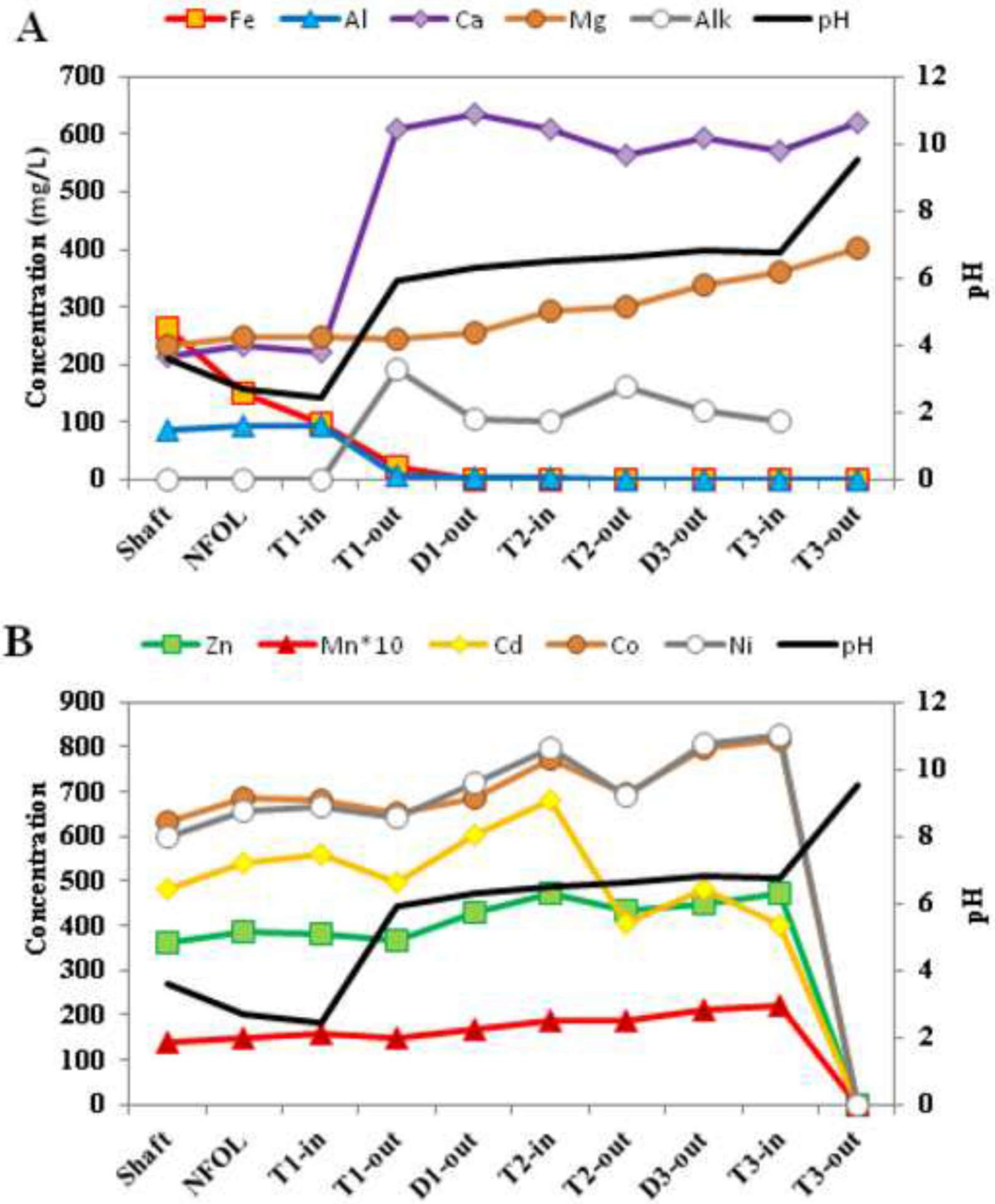
A
Fe
Al
Ca
Mg
Alk
pH
Concentration (mg/L)
700
600
500
400
300
200
100
0
12
10
8
6
4
2
0
pH
Shaft
NFOL
T1-in
T1-out
D1-out
T2-in
T2-out
D3-out
T3-in
T3-out
B
Zn
Mn*10
Cd
Co
Ni
pH
Concentration
900
800
700
600
500
400
300
200
100
0
12
10
8
6
4
2
0
pH
Shaft
NFOL
T1-in
T1-out
D1-out
T2-in
T2-out
D3-out
T3-in
T3-out

Figure 3

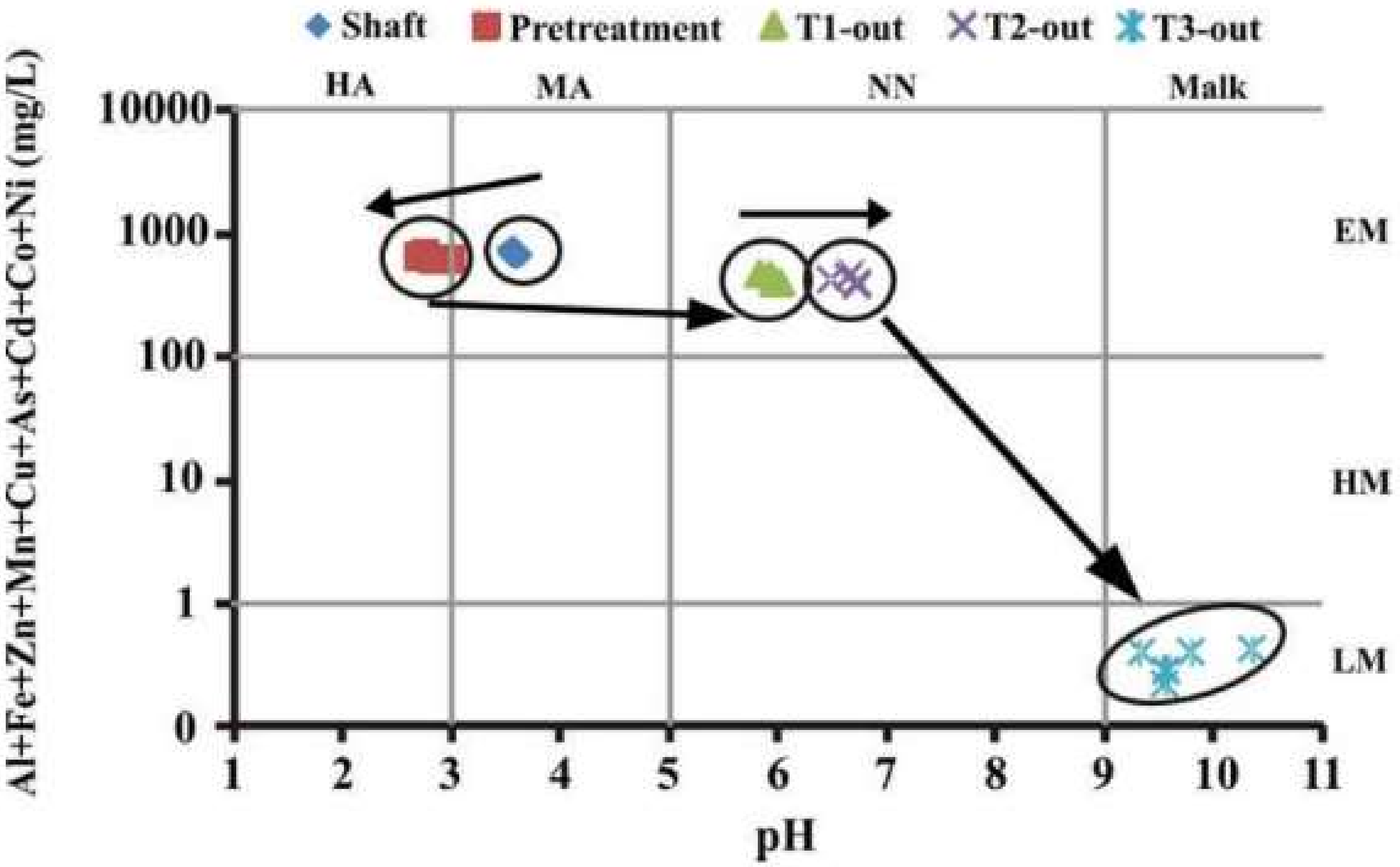
◆ Shaft
■ Pretreatment
▲ T1-out
× T2-out
✱ T3-out
HA
MA
NN
Malk
EM
HM
LM
10000
1000
100
10
1
0
1
2
3
4
5
6
7
8
9
10
11
pH
Al+Fe+Zn+Mn+Cu+As+Cd+Co+Ni (mg/L)

Figure 4

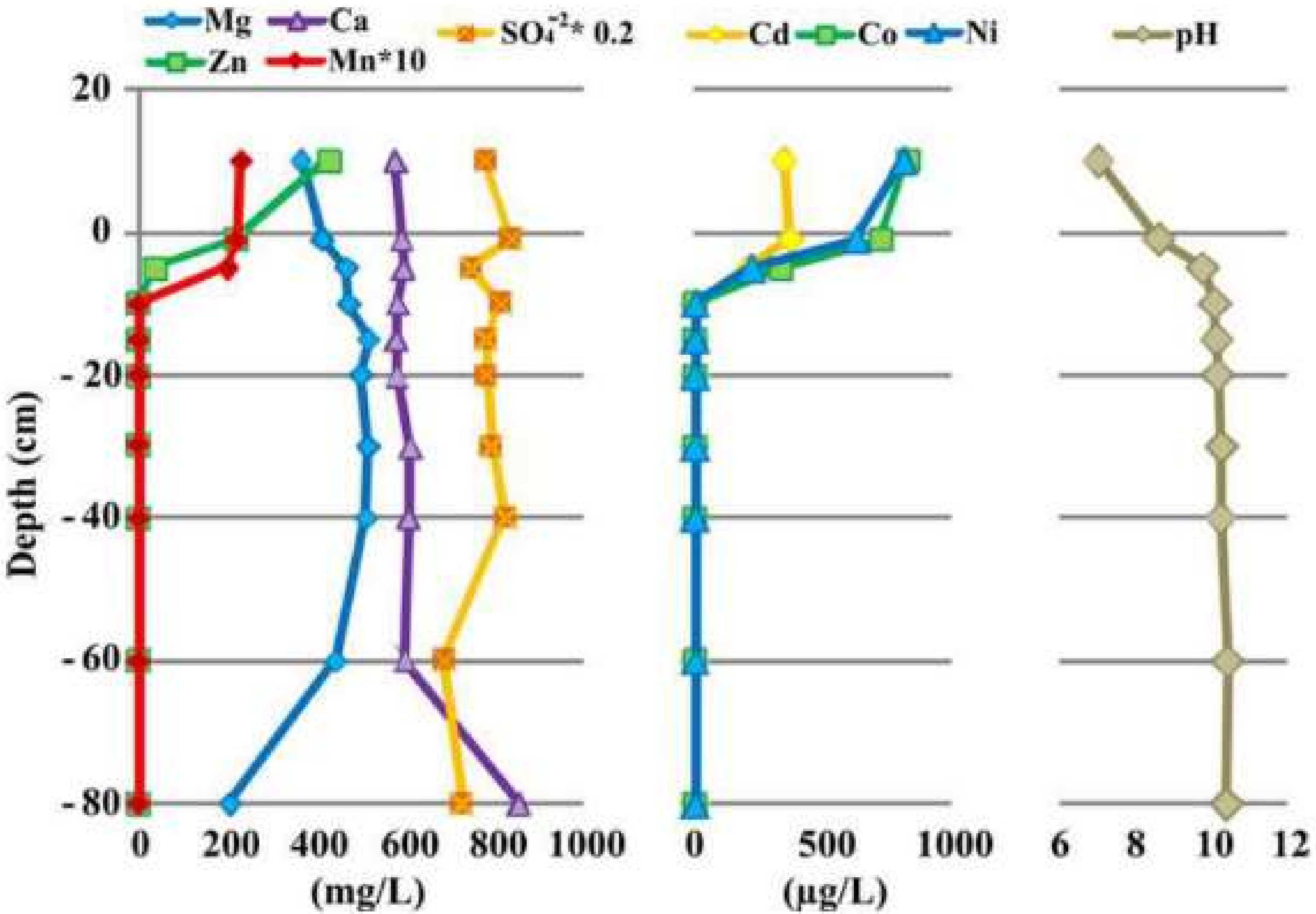
Mg
Ca
Zn
Mn*10
SO_4^{-2}* 0.2
Cd
Co
Ni
pH
Depth (cm)
20
0
- 20
- 40
- 60
- 80
0
200
400
600
800
1000
(mg/L)
0
500
1000
(µg/L)
6
8
10
12

Figure 5

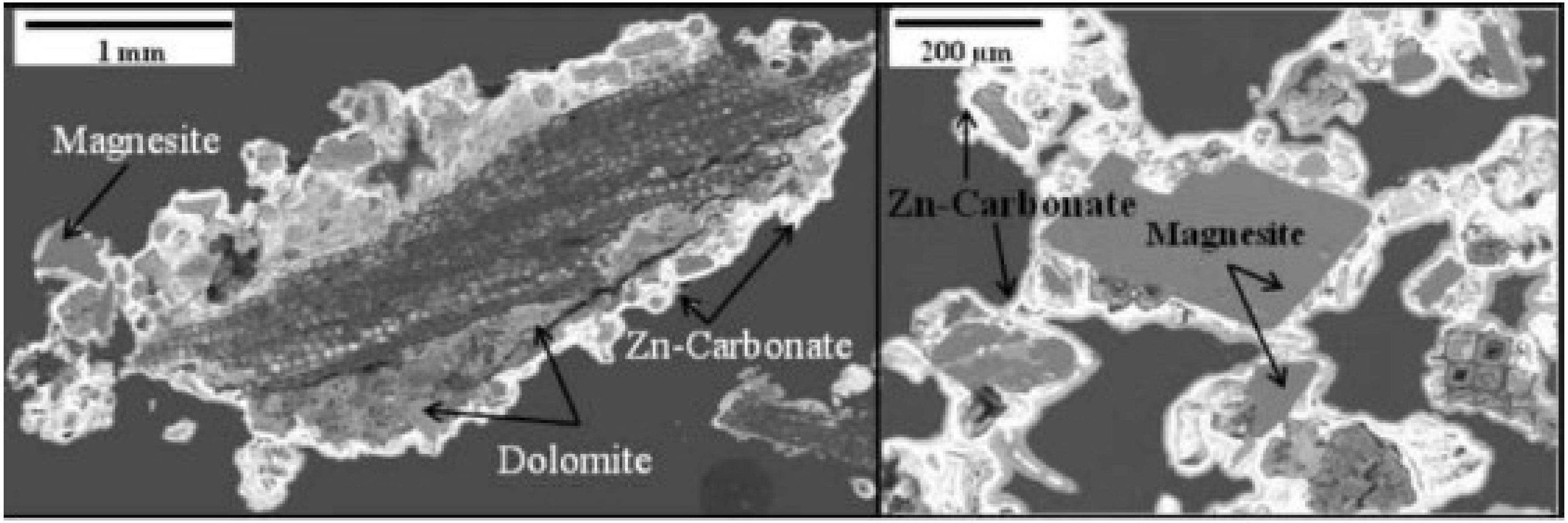
1 mm
Magnesite
Zn-Carbonate
Dolomite
200 µm
Zn-Carbonate
Magnesite

Figure 6

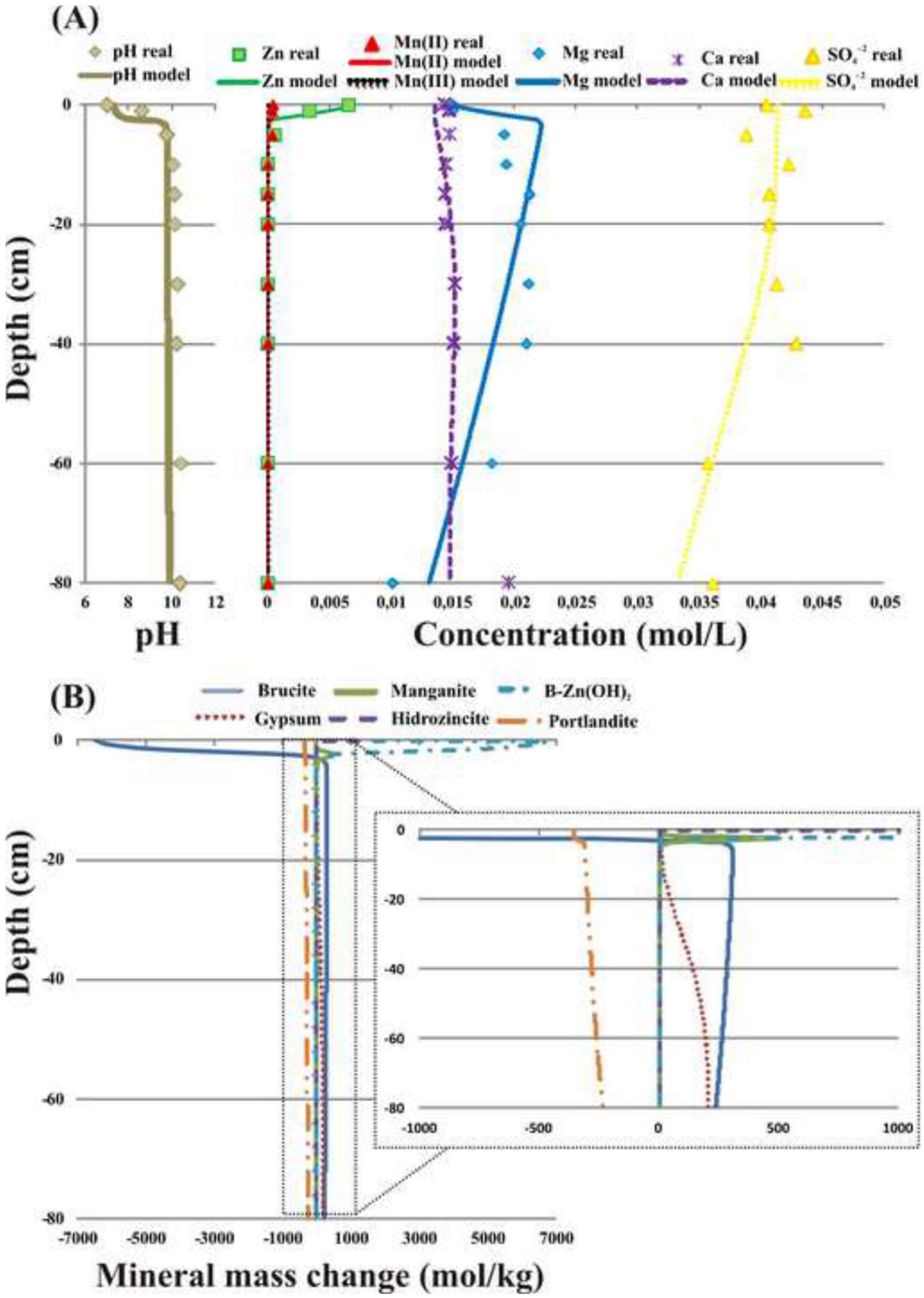
(A)
pH real
pH model
Zn real
Zn model
Mn(II) real
Mn(II) model
Mn(III) model
Mg real
Mg model
Ca real
Ca model
SO_4^{-2} real
SO_4^{-2} model
0
-20
-40
-60
-80
Depth (cm)
6
8
10
12
pH
0
0,005
0,01
0,015
0,02
0,025
0,03
0,035
0,04
0,045
0,05
Concentration (mol/L)
(B)
Brucite
Manganite
B-Zn(OH)$_2$
Gypsum
Hidrozincite
Portlandite
0
-20
-40
-60
-80
Depth (cm)
-7000
-5000
-3000
-1000
1000
3000
5000
7000
Mineral mass change (mol/kg)
0
-20
-40
-60
-80
-1000
-500
0
500
1000

Table 1

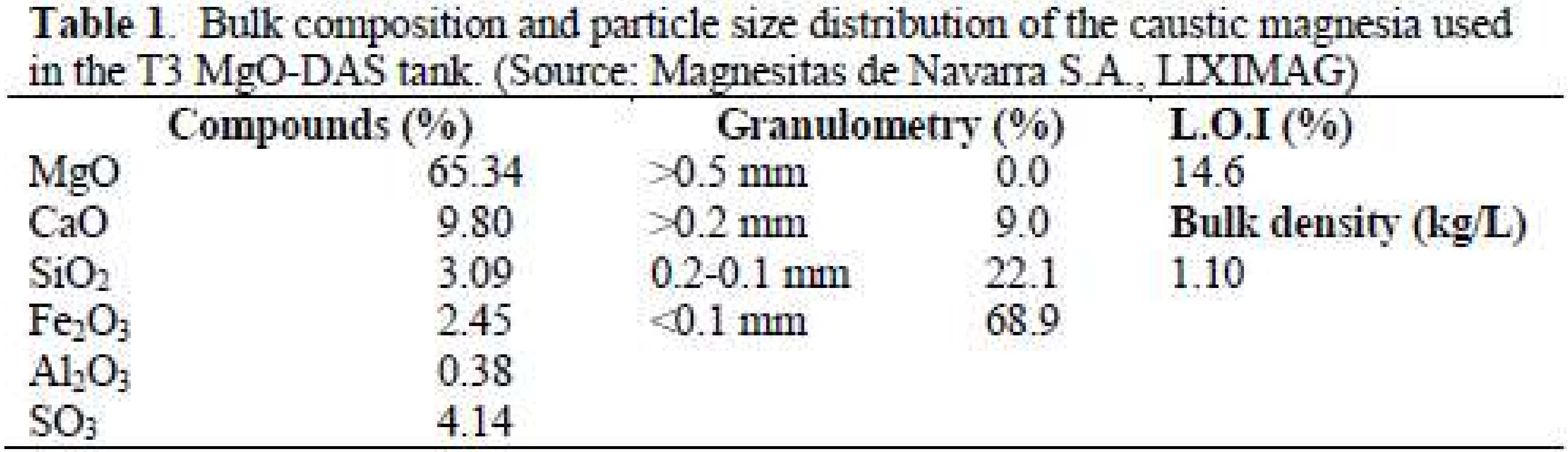

Table 1. Bulk composition and particle size distribution of the caustic magnesia used in the T3 MgO-DAS tank. (Source: Magnesitas de Navarra S.A., LIXIMAG)

Compounds (%)		**Granulometry (%)**		**L.O.I (%)**
MgO	65.34	>0.5 mm	0.0	14.6
CaO	9.80	>0.2 mm	9.0	**Bulk density (kg/L)**
SiO_2	3.09	0.2-0.1 mm	22.1	1.10
Fe_2O_3	2.45	<0.1 mm	68.9	
Al_2O_3	0.38			
SO_3	4.14			

Table 2

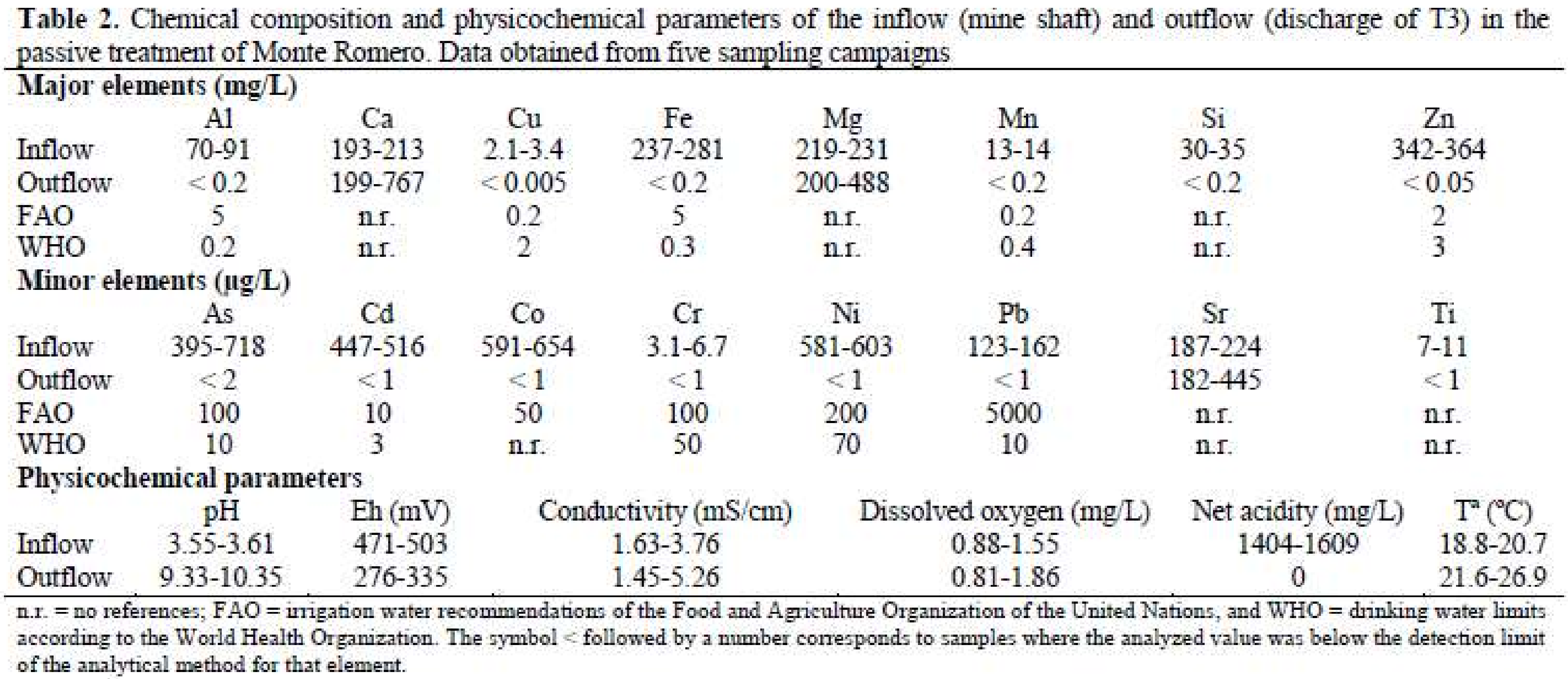

Table 2. Chemical composition and physicochemical parameters of the inflow (mine shaft) and outflow (discharge of T3) in the passive treatment of Monte Romero. Data obtained from five sampling campaigns

Major elements (mg/L)								
	Al	Ca	Cu	Fe	Mg	Mn	Si	Zn
Inflow	70-91	193-213	2.1-3.4	237-281	219-231	13-14	30-35	342-364
Outflow	< 0.2	199-767	< 0.005	< 0.2	200-488	< 0.2	< 0.2	< 0.05
FAO	5	n.r.	0.2	5	n.r.	0.2	n.r.	2
WHO	0.2	n.r.	2	0.3	n.r.	0.4	n.r.	3
Minor elements (µg/L)								
	As	Cd	Co	Cr	Ni	Pb	Sr	Ti
Inflow	395-718	447-516	591-654	3.1-6.7	581-603	123-162	187-224	7-11
Outflow	< 2	< 1	< 1	< 1	< 1	< 1	182-445	< 1
FAO	100	10	50	100	200	5000	n.r.	n.r.
WHO	10	3	n.r.	50	70	10	n.r.	n.r.

Physicochemical parameters						
	pH	Eh (mV)	Conductivity (mS/cm)	Dissolved oxygen (mg/L)	Net acidity (mg/L)	Tª (ºC)
Inflow	3.55-3.61	471-503	1.63-3.76	0.88-1.55	1404-1609	18.8-20.7
Outflow	9.33-10.35	276-335	1.45-5.26	0.81-1.86	0	21.6-26.9

n.r. = no references; FAO = irrigation water recommendations of the Food and Agriculture Organization of the United Nations, and WHO = drinking water limits according to the World Health Organization. The symbol < followed by a number corresponds to samples where the analyzed value was below the detection limit of the analytical method for that element.

Table 3

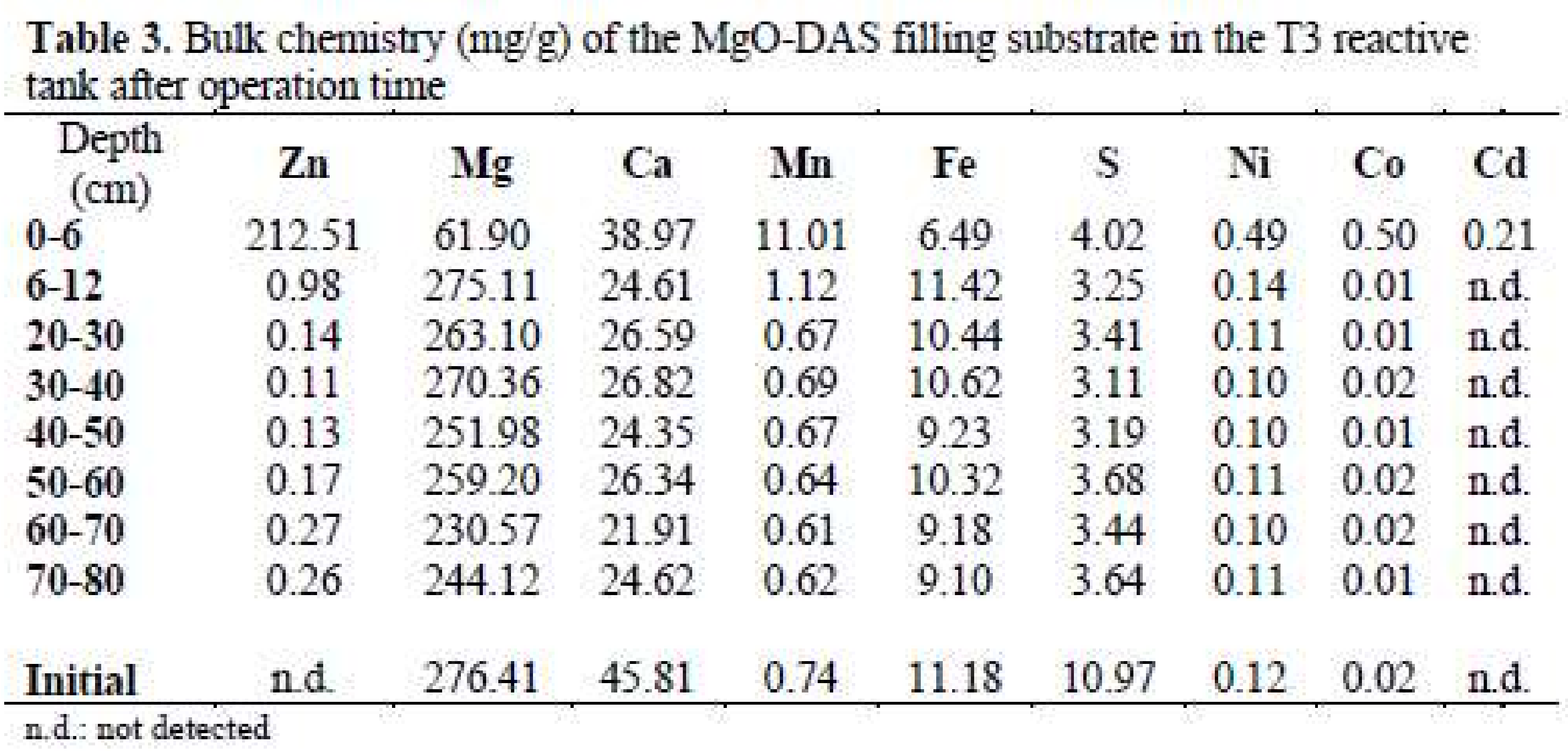

Table 3. Bulk chemistry (mg/g) of the MgO-DAS filling substrate in the T3 reactive tank after operation time

Depth (cm)	Zn	Mg	Ca	Mn	Fe	S	Ni	Co	Cd
0-6	212.51	61.90	38.97	11.01	6.49	4.02	0.49	0.50	0.21
6-12	0.98	275.11	24.61	1.12	11.42	3.25	0.14	0.01	n.d.
20-30	0.14	263.10	26.59	0.67	10.44	3.41	0.11	0.01	n.d.
30-40	0.11	270.36	26.82	0.69	10.62	3.11	0.10	0.02	n.d.
40-50	0.13	251.98	24.35	0.67	9.23	3.19	0.10	0.01	n.d.
50-60	0.17	259.20	26.34	0.64	10.32	3.68	0.11	0.02	n.d.
60-70	0.27	230.57	21.91	0.61	9.18	3.44	0.10	0.02	n.d.
70-80	0.26	244.12	24.62	0.62	9.10	3.64	0.11	0.01	n.d.
Initial	n.d.	276.41	45.81	0.74	11.18	10.97	0.12	0.02	n.d.

n.d.: not detected

Table 4

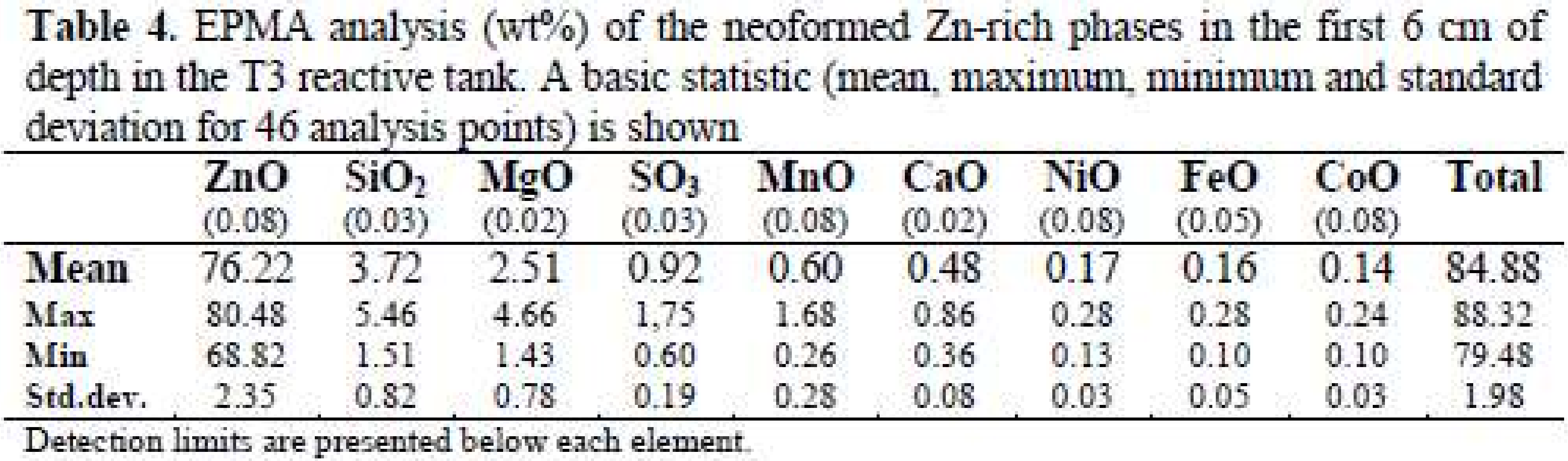

Table 4. EPMA analysis (wt%) of the neoformed Zn-rich phases in the first 6 cm of depth in the T3 reactive tank. A basic statistic (mean, maximum, minimum and standard deviation for 46 analysis points) is shown

	ZnO (0.08)	SiO_2 (0.03)	MgO (0.02)	SO_3 (0.03)	MnO (0.08)	CaO (0.02)	NiO (0.08)	FeO (0.05)	CoO (0.08)	Total
Mean	76.22	3.72	2.51	0.92	0.60	0.48	0.17	0.16	0.14	84.88
Max	80.48	5.46	4.66	1,75	1.68	0.86	0.28	0.28	0.24	88.32
Min	68.82	1.51	1.43	0.60	0.26	0.36	0.13	0.10	0.10	79.48
Std.dev.	2.35	0.82	0.78	0.19	0.28	0.08	0.03	0.05	0.03	1.98

Detection limits are presented below each element.

Table 5

Table 5: Kinetic-equilibrium reactions and initial reactive surface of the MgO-DAS used in the reactive transport model

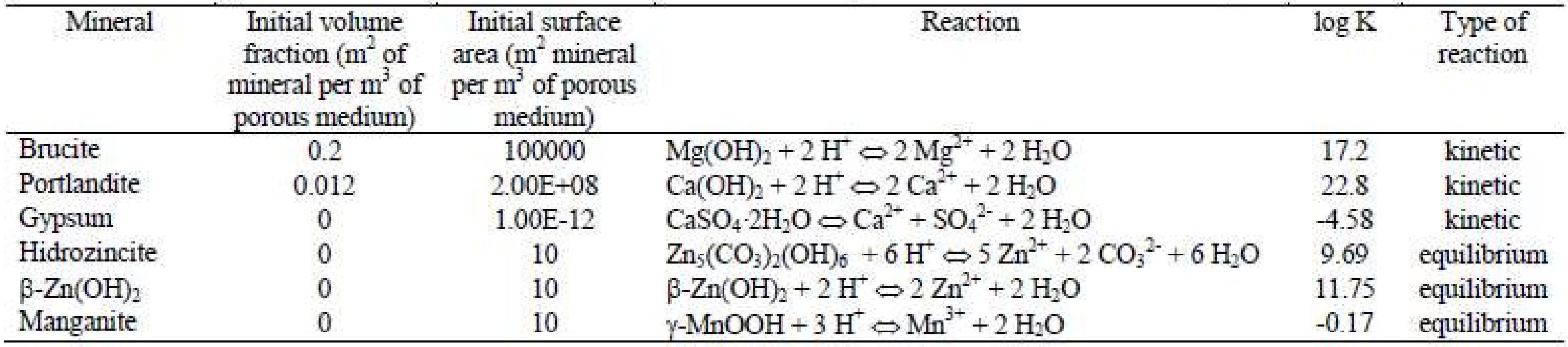

Mineral	Initial volume fraction (m^2 of mineral per m^3 of porous medium)	Initial surface area (m^2 mineral per m^3 of porous medium)	Reaction	log K	Type of reaction
Brucite	0.2	100000	$Mg(OH)_2 + 2 H^+ \Leftrightarrow 2 Mg^{2+} + 2 H_2O$	17.2	kinetic
Portlandite	0.012	2.00E+08	$Ca(OH)_2 + 2 H^+ \Leftrightarrow 2 Ca^{2+} + 2 H_2O$	22.8	kinetic
Gypsum	0	1.00E-12	$CaSO_4 \cdot 2H_2O \Leftrightarrow Ca^{2+} + SO_4^{2-} + 2 H_2O$	-4.58	kinetic
Hidrozincite	0	10	$Zn_5(CO_3)_2(OH)_6 + 6 H^+ \Leftrightarrow 5 Zn^{2+} + 2 CO_3^{2-} + 6 H_2O$	9.69	equilibrium
β-$Zn(OH)_2$	0	10	$\beta\text{-}Zn(OH)_2 + 2 H^+ \Leftrightarrow 2 Zn^{2+} + 2 H_2O$	11.75	equilibrium
Manganite	0	10	$\gamma\text{-}MnOOH + 3 H^+ \Leftrightarrow Mn^{3+} + 2 H_2O$	-0.17	equilibrium